ACS APPLIED BIO MATERIALS

www.acsabm.org
Article

AFM-Based Single-Molecule Force Spectroscopy of PEG−Anti-PEG Antibody Interactions

Glenn Villena Latag, Hiroyuki Tahara, Airi Katase, Shoichi Maeda, Yiwei Liu, Yoshimitsu Kakuta, Takamasa Teramoto, Takeshi Mori,* and Tomohiro Hayashi*

Cite This: ACS Appl. Bio Mater. 2026, 9, 1450−1462

ABSTRACT: Poly(ethylene glycol) (PEG) is widely used as a stealth polymer to enhance drug stability and circulation by reducing immune recognition. However, anti-PEG antibodies are increasingly reported in humans, leading to accelerated drug clearance and adverse immune responses. While ensemble assays have clarified the scheme of PEG−antibody binding, they lack the resolution to probe molecular-scale mechanics. Here, we used atomic force microscopy-based single-molecule force spectroscopy (AFM-SMFS) to examine how PEG terminal chemistry and antibody maturation modulate these interactions. Methoxy- (m-PEG) and hydroxy-terminated PEG (HO-PEG) were tested against Fv-clasps from two anti-PEG IgMs: the naïve IgM M9 and the affinity-matured IgM M11. M11 bound PEG more strongly and at shorter rupture distances than M9, with 2D force−distance maps revealing the most intense signatures for M11 and m-PEG pair. Complementary quartz crystal microbalance with dissipation (QCM-D) and Fourier-transform infrared (FTIR) spectroscopy confirmed higher binding by M11 and a terminal preference of M9 for m-PEG. In addition to antibody maturation, we report that the hydrated structure of PEG plays a significant role in PEG−antibody binding. HO-PEG forms extended, hydrated layers, whereas m-PEG adopts compact, collapsed conformations, shaping antibody accessibility and binding mechanics. These results provide molecular-level insight into how antibody structure and PEG hydration state dictate binding, offering design principles for PEGylated therapeutics with reduced immunogenicity and improved performance.

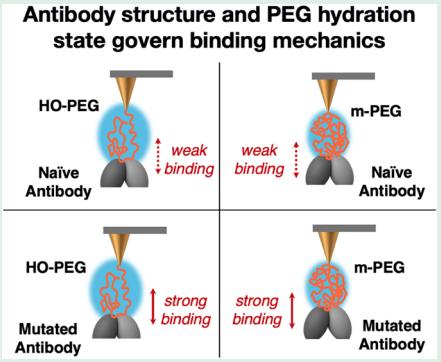

KEYWORDS: *PEG, anti-PEG antibody, single molecule force spectroscopy, atomic force microscopy, FTIR spectroscopy, QCM-D*

INTRODUCTION

Prolonged circulation of therapeutic agents in the bloodstream is essential to maintain effective drug concentrations at target tissues.[1−3] However, protein-based drugs and nanoparticle carriers are often rapidly cleared due to immune recognition and degradation.[4−6] To address this challenge, hydrophilic "stealth" polymers are commonly used as surface coatings to enhance systemic circulation, reduce immunogenicity, and improve drug stability.[7−9] Among these polymers, poly(ethylene glycol) (PEG) is the most widely adopted in drug delivery systems due to its excellent biocompatibility, hydrophilicity, and tunable molecular architecture.[10−15] When grafted onto therapeutic surfaces, PEG forms a dense, brush-like steric barrier that minimizes opsonization and subsequent clearance by the immune system.[16−19] Nevertheless, despite its widespread use and historical classification as nonimmunogenic, accumulating evidence has revealed that PEG can elicit immune responses, particularly through the induction of anti-PEG antibodies.[20−24] These antibodies can recognize and bind PEG-modified therapeutics, resulting in accelerated blood clearance and reduced pharmacological efficacy.[25−29]

To better understand the molecular basis of these immune responses, several analytical techniques have been employed to characterize how anti-PEG antibodies interact with PEG. Techniques like surface plasmon resonance (SPR), enzyme-linked immunosorbent assays (ELISA), and X-ray crystallography have revealed PEG-binding motifs in affinity-matured antibodies.[26,27,30−36] However, these studies mainly reflect T cell-dependent (TD) responses and not the initial recognition by naive B cell receptors (BCRs).[30,37] In contrast, PEG-modified therapeutics without protein components often induce IgM responses via the T cell-independent (TI) pathway, which lacks affinity maturation.[38−40] Studying these TI-induced IgMs offers a more accurate view of how naïve BCRs engage PEG, which is essential for designing PEGylated drugs with reduced immunogenicity. More importantly, while this type of antibody response helps explain the origins of anti-PEG immunity, addressing the broader challenges of PEG immunogenicity requires a detailed understanding of the weak,

Received: October 6, 2025
Revised: December 4, 2025
Accepted: December 4, 2025
Published: January 20, 2026

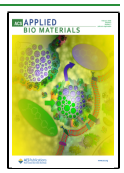

transient, and heterogeneous interactions that underlie PEG–antibody recognition.[34,41−43] These subtle features are often masked in ensemble-averaged measurements and are best resolved using single-molecule techniques.

Atomic force microscopy-based single-molecule force spectroscopy (AFM-SMFS) has emerged as a powerful tool for probing biomolecular interactions,[44−47] including antigen–antibody binding.[48−51] By applying controlled forces in the piconewton range, AFM-SMFS enables direct measurement of unbinding forces and dissociation kinetics for individual binding events. This technique is particularly well suited for characterizing the weak and dynamic interactions involved in PEG–anti-PEG antibody recognition. Furthermore, comparisons of force signatures across PEGs with different molecular weights[33] or terminal functional groups, such as hydroxy versus methoxy end groups,[22,52,53] can reveal structural features that influence antibody binding.[54,55]

In this study, we employed AFM-SMFS to investigate the unbinding behavior between anti-PEG antibodies and PEG molecules at the single-molecule level. Naïve (TI) and mutated (TD) monovalent anti-PEG Fv-clasps were immobilized on chemically modified gold-coated silicon substrates, while AFM cantilever tips were functionalized with thiol-terminated PEGs bearing either hydroxy or methoxy end groups. Fv-clasp is an engineered Fv construct in which heavy- and light-chain variable domains (V_H and V_L) are paired through a stabilizing coiled-coil template. Because the coiled-coil is fused to the C-termini—away from the antigen-binding interface—it does not interfere with antigen recognition, unlike in some scFv formats where the V_H–V_L linker can alter binding. Because IgM carries ten antigen-binding sites, multivalent engagement varies among binding events and generates avidity effects that obscure intrinsic affinity. To isolate single-molecule interactions, we used a monovalent Fv-clasp construct, which enables evaluation of intrinsic affinity through single-bond mechanics. We focused on analyzing the distributions of adhesion forces and rupture distances to capture the heterogeneity in molecular interactions. We quantified binding strengths and spatial characteristics through systematic force mapping and statistical analysis of rupture events. Ensemble techniques including QCM-D and FTIR were also performed to support the findings on antibody–PEG binding and to characterize the hydrated structure of PEG, which may play a significant role in modulating the binding mechanism. We believe that these findings will reveal important insights on how the immune system recognizes PEG and offer practical guidance for designing new PEGylated drugs that are less likely to trigger immune responses.

MATERIALS AND METHODOLOGY

Si Substrate Preparation

SiO_2 wafers were cut into 1 cm^2 pieces using a diamond cutter. The substrates were precleaned by UV/ozone treatment for 15 min, followed by sequential ultrasonication in acetone, ethyl alcohol, and deionized water. After drying, the wafers were subjected to a second UV/ozone treatment for 15 min and briefly immersed in absolute ethanol with occasional shaking to reduce surface oxides. The substrates were then dried under a stream of nitrogen. A 50 nm Ge adhesion layer and a 300 nm Au layer were deposited onto the cleaned wafers using thermal evaporation in a custom-built high-vacuum chamber. The gold-coated Si substrates were stored under vacuum until use.

Self-Assembled Monolayers (SAMs) Preparation

Mixed SAMs were prepared by immersing Au-coated Si substrates in ethanolic thiol solutions containing 1 mM carboxy-terminated (COOH) and sulfobetaine-terminated (SB) thiols at a 1:10 molar ratio, as summarized in Table 1. The data for octanethiol (C8) SAMs is included in the table for comparison. Prior to thiol immersion, the substrates were briefly subjected to UV/ozone treatment for 15 min, followed by rinsing with absolute ethanol to stabilize surface oxides and minimize interference with SAM formation.[56] After overnight immersion, the substrates were rinsed with ethanol and dried under nitrogen.

Table 1. A List of SAMs Fabricated with Their Corresponding Precursor Molecules, Static Water Contact Angles, and Density Relative to Alkanethiols

Notation for SAMs (based on the terminal group)	The molecular formula of precursor	Static water contact angle (°)	Density with respect to alkanethiols
C8[a]	$HS(CH_2)_7CH_3$	112 (3.1)[c]	—
COOH[b]	$HS(CH_2)_{11}COOH$	18 (4.4)[c]	95 (2.0)[c]
SB[a]	$HS(CH_2)_{11}N^+(CH_3)_2CH_2SO_3^-$	39.6 (3.9)[c]	59.5 (0.72)[d]

[a]Purchased from Sigma-Aldrich and. [b]ProChimia surfaces. Numbers in parentheses are standard deviations. [c]n = 5. [d]n = 12. Data reproduced from Hayashi et al.[57]

Preparation of Anti-PEG IgM Fv-Clasp

Anti-PEG IgM clones M9 and M11 were kindly provided by Dr. Tatsuhiro Ishida (Tokushima University). Fv-clasps (chimeric antibody fragments of ∼37 kDa) of M9 and M11 were prepared based on our previous report.[38] Briefly, synthetic cDNAs encoding M9 and M11 Fv-clasps, with SARAH domains fused to the V_H and V_L cassettes as described previously,[58] were subcloned into pE His vectors containing an N-terminal Ser–Lys–Ile–Lys–His_6 tag. V_H–SARAH and V_L–SARAH were expressed separately in *E. coli* BL21-CodonPlus (DE3)-RIL (Agilent Technologies), induced at OD_{600} 0.4–0.6 with 0.5 mM IPTG overnight at 36 °C. Cells were harvested, lysed in 50 mM Tris–HCl, 500 mM NaCl (pH 8.0), and inclusion bodies were isolated and solubilized in 6 M guanidine–HCl, 50 mM Tris, 150 mM NaCl, and 375 μM β-mercaptoethanol (pH 8.0). Denatured V_H and V_L chains were mixed at equimolar ratios and refolded by sequential dilution into buffers containing 4 M urea/0.4 M L-arginine and then 0.4 M L-arginine, both with 375 μM oxidized glutathione, 50 mM Tris–HCl, and 150 mM NaCl (pH 8.0). Refolded proteins were purified by ion exchange chromatography (Superdex 200, Cytiva) in 50 mM Tris–HCl, 150 mM NaCl (pH 8.0), followed by anion exchange (HiTrap Q) with a linear 0–1 M NaCl gradient in 20 mM Tris (pH 7.5). Peak fractions were pooled and concentrated to 8.8 mg/mL (M9) and 11 mg/mL (M11).

Fv-Clasp Immobilization

COOH/SB-functionalized Au-coated Si substrates were activated by immersion in a freshly prepared 1:1 (v/v) solution of 300 mM *N*-hydroxysuccinimide (NHS) (TCI, Tokyo, Japan) and 100 mM *N*-(3-(dimethylamino)propyl)-*N*′-ethylcarbodiimide (EDC) (Sigma-Aldrich, St. Louis, MO, USA) in phosphate-buffered saline (PBS) for 30 min. After activation, substrates were rinsed five times with PBS to remove unreacted reagents. The NHS/EDC treatment enables covalent coupling of antibody Fv-clasps via carboxyl groups on the COOH SAMs, while SB moieties provide antifouling functionality. The substrates were then incubated in 0.9 mg/mL solutions of M9 or M11 Fv-clasps in PBS for 8 h at room temperature. Following Fv-clasp immobilization, the substrates were rinsed three times with PBS to remove unbound antibody Fv-clasps. The substrates were stored in

https://doi.org/10.1021/acsabm.5c01967
ACS Appl. Bio Mater. 2026, 9, 1450−1462

sealed, humidified glass containers prior to AFM analysis to prevent drying.

Cantilever Tip Functionalization

BioLever mini cantilevers (Olympus, Tokyo, Japan; nominal spring constant: 0.09 N/m) were coated with 25 nm of Ge followed by 150 nm of Au via thermal evaporation. Thiol-terminated methoxy-PEG (m-PEG, MW = 2000 Da; Biopharma PEG Scientific Inc., MA, USA) and hydroxy-PEG (HO-PEG, MW = 2000 Da; Biopharma PEG Scientific Inc., MA, USA) were each dissolved in PBS to prepare 1 mg/mL solutions. Cantilevers were mounted on metal holders and immersed in 1 mL of the respective thiol solutions for 24 h. After incubation, the tips were rinsed thoroughly with PBS to remove physisorbed PEG molecules. The molecular structures of HO-PEG and m-PEG used in this study are shown in Figure 1.

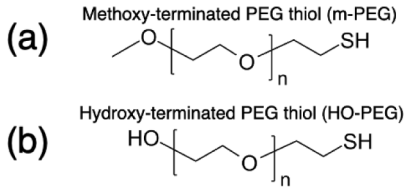

Figure 1. Molecular structures of m-PEG and HO-PEG alkanethiols used in the study. Both molecules consist of a polyethylene glycol chain ($n \approx 45$ ethylene oxide units) terminated with either a (a) methoxy or (b) hydroxy functional group, and a thiol group for gold surface anchoring.

AFM-Based SMFS Measurements

SMFS experiments have been used to quantify the unbinding forces between ligands and receptors through a method described by Butt et al.[59] Figure 2 shows a typical force−separation curve acquired from an AFM experiment employing a PEG-functionalized tip and anti-PEG antibody Fv-clasps immobilized on the mixed SB/COOH SAM surface. The functionalized cantilever probe is driven to travel a vertical separation distance as indicated by the noncontact region of the approach phase. Then, the probe experiences a positive deflection as it comes into contact with the substrate. Upon reaching a set trigger force, the probe retracts and experiences a pulling force (adhesion force) due to the sum of van der Waals and electrostatic forces between the antibody and the PEG molecules. A minimum value, called rupture force, is commonly used as an estimate of the largest unbinding force of the PEG−anti-PEG antibody reaction pathway.

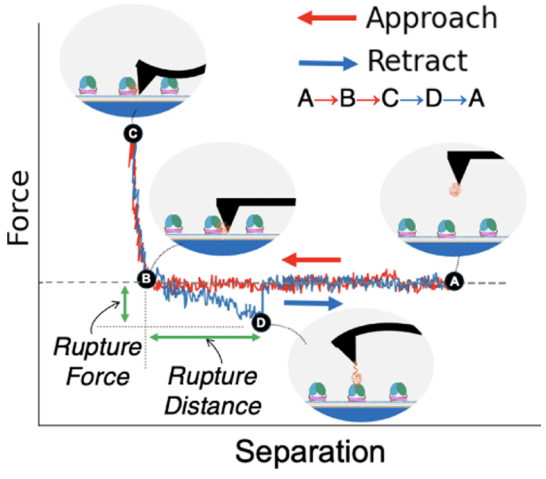

Figure 2. Representative force−separation curve acquired from AFM-based SMFS. The *x*-axis denotes the tip−sample separation, and the *y*-axis shows the measured force. The red curve represents the approach phase, while the blue curve corresponds to the retraction phase. Key stages in the force curve are labeled as follows: (A) noncontact region, where no interaction is detected; (B) contact point, where the cantilever tip first contacts the surface; (C) trigger point, where a defined loading force is reached prior to retraction; and (D) rupture point, corresponding to the minimum force during retraction (rupture force) and the corresponding tip−sample separation (rupture distance), which indicates the unbinding event between the PEG and the anti-PEG antibody Fv-clasp.

Force−separation curves were acquired using a commercial atomic force microscope equipped with a liquid cell (MFP-3D Infinity, Oxford Instruments, U.K.). Force maps (10 μm^2) were initially recorded to locate Fv-clasp-immobilized regions. Subsequently, conventional force−distance measurements were performed at each region ($n \geq 3$) or until Fv-clasp signals were no longer detectable due to thermal drift. Cantilever tips functionalized with thiol-terminated PEG were approached to the substrate surface at a constant rate of 150 nm/s. The spring constants of the cantilevers were calibrated using the thermal noise method.

A series of exhaustive force mapping measurements were undertaken to determine the locations of Fv-clasps immobilized onto the Au-coated Si substrate. Figure 3a shows a representative force map acquired over a small area in the substrate. Careful consideration was taken in choosing the optimal antibody concentration, typically in the range of 0.5−1.0 mg/mL.[60] An amount greater than the optimal value may result in simultaneous binding events between multiple antigen and antibody molecules, which will make the deconvolution of the force curves difficult. On the other hand, concentrations lower than the optimal value may result in very few binding sites, which will greatly lessen the probability of unbinding events. Details on this preliminary determination of the optimal antibody concentration are shown in the associated content (Supporting Information S1). The force curves without adhesion events (Figure 3b) were rejected from the analysis while force curves with valid adhesion events (Figure 3c) were further analyzed to extract the adhesion force and rupture distances. Hundreds of force curves with adhesion events were used to construct 2D visualization plots.

Force and Rupture Distance Data Analysis

Adhesion force and rupture distance values were extracted from single-molecule AFM retraction curves. Data for each antibody−PEG pair (M9 + OH-PEG, M9 + m-PEG, M11 + OH-PEG, M11 + m-PEG) were processed using custom Python scripts (Python v3.10). Force histograms and rupture distance histograms were normalized to reflect percent distribution. To assess uncertainty in the mean values, 10,000 bootstrap resamples were used to estimate 95% confidence intervals. To gain deeper insight into the joint distribution of adhesion force and rupture distance, two-dimensional kernel density estimation (2D-KDE) was performed using the gaussian_kde function (SciPy) and visualized with Seaborn. Data from all force curves with adhesion events per condition were pooled, and a bivariate KDE was computed. KDE maps were evaluated over a grid of 200 × 200 points. From each KDE map, the global maximum (peak) was identified to determine the most probable rupture event, while mean values were calculated directly from the raw distributions. The hotspot area, defined as the spatial region where the KDE exceeded 50% of the maximum density, was computed by numerical integration across the force−distance grid.

QCM-D Measurements

HO-PEG and m-PEG SAM-functionalized Au-coated quartz sensors were mounted into the flow modules of a commercial QCM-D system (Biolin Scientific AB, Gothenburg, Sweden). A series of solutions were introduced into the modules using a peristaltic pump (Minato, Tokyo, Japan) at a constant flow rate of 50 μL/s throughout the experiment. The changes in frequency shifts (Δf) and energy dissipation (ΔD) were recorded over the following time course: (i) establishment of a stable baseline in phosphate-buffered saline (PBS), (ii) injection of anti-PEG antibody Fv-clasp solution in PBS until signal stabilization (~60 min), and (iii) rinsing with PBS until the

https://doi.org/10.1021/acsabm.5c01967
ACS Appl. Bio Mater. 2026, 9, 1450−1462

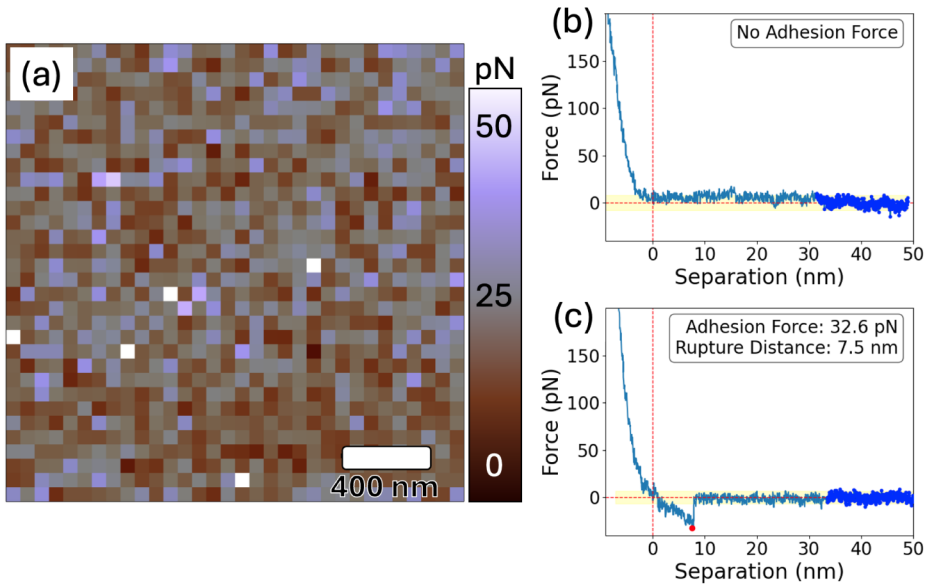

Figure 3. Representative adhesion force map and example force curves. (a) Adhesion force map acquired over a small area of the substrate using AFM-based SMFS. Regions of higher adhesion forces are indicated by purple or white tones, while lower adhesion forces appear in darker brown to black shades. (b) A representative force−distance curve showing no detectable adhesion event. (c) A representative curve exhibiting a clear adhesion event, characterized by a distinct rupture force during the retraction phase. The bright blue points were used to establish the zero-force baseline, and the yellow band denotes the noise band.

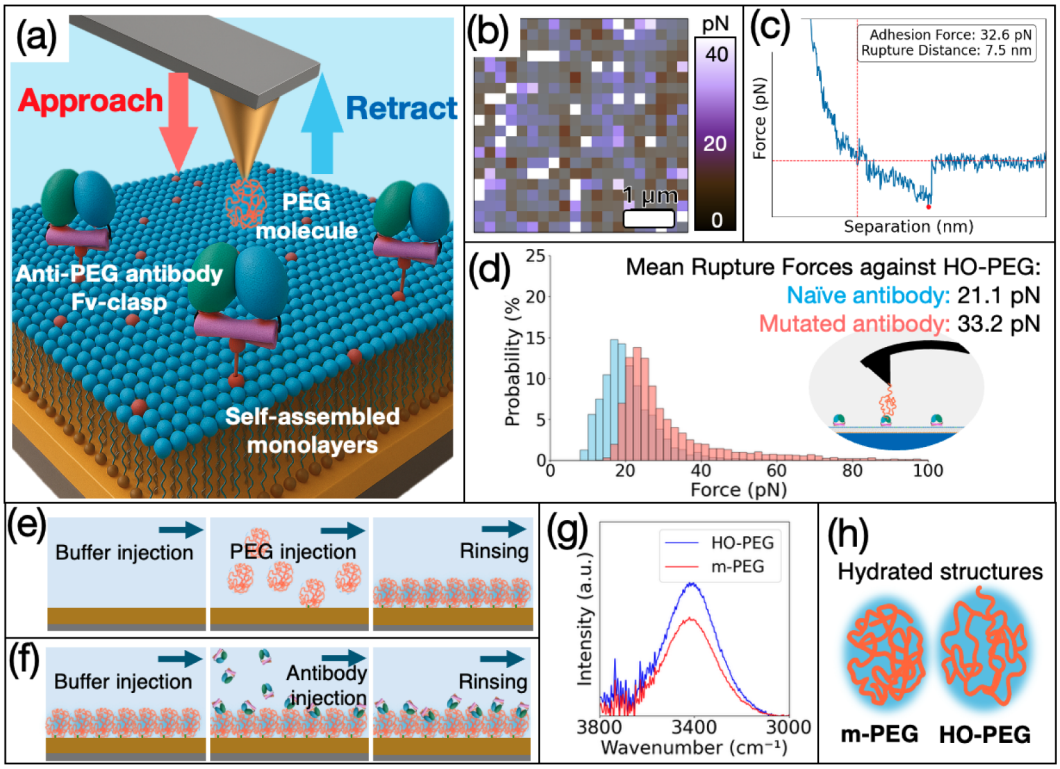

Figure 4. Overview of this work. (a) Artistic representation of the AFM-SMFS setup, with anti-PEG antibody Fv-clasps immobilized on self-assembled monolayers (SAMs) and the AFM cantilever functionalized with HO-PEG or m-PEG. The probe was driven in approach−retract cycles to measure PEG−antibody rupture forces and distances. (b) Representative force map with adhesion events highlighted in white/purple pixels and (c) example retraction curve with valid adhesion event representing the highlighted pixels. (d) Rupture forces and distances were pooled, and mean values for naïve (M9) and mutated (M11) antibodies with HO-PEG or m-PEG were compared using histograms. Ensemble measurements included are (e) QCM-D to monitor PEG layer formation and hydration and (f) assess antibody binding, and (g) FTIR spectroscopy to probe hydration dynamics through OH stretching bands. (h) These results suggests that HO-PEG and m-PEG adopt distinct hydration structures, which in turn shape their interactions with naïve and mutated anti-PEG antibodies.

signal stabilized once again, as described from our previous report.[61] For both M9 and M11, PEG SAM-coated substrates were incubated with antibody solutions at 0.1 mg/mL to ensure comparable antibody:PEG ratios across experiments. Equilibrium Δf (Hz) and

https://doi.org/10.1021/acsabm.5c01967
ACS Appl. Bio Mater. 2026, 9, 1450−1462

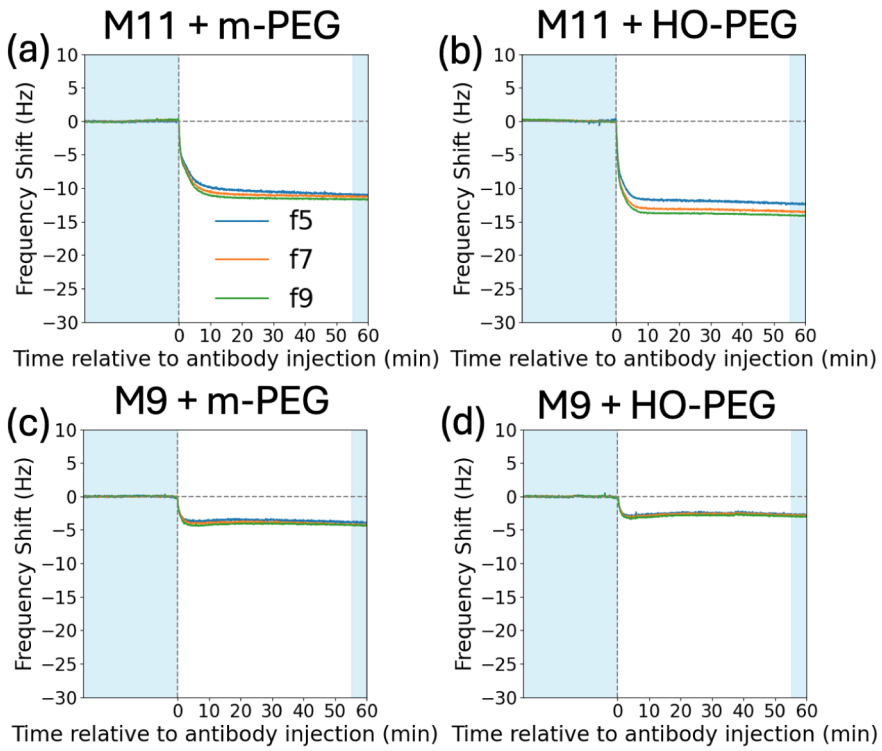

Figure 5. Representative real-time Δf at overtones 5, 7, and 9 for all four Fv-clasp and PEG pairings: (a) M11 + m-PEG, (b) M11 + HO-PEG, (c) M9 + m-PEG, and (d) M9 + HO-PEG. The light blue band at the beginning indicates the establishment of the PBS baseline, while the band on the right marks the rinsing phase with PBS to remove unbound antibody Fv-clasps.

ΔD (ppm) were calculated as the difference between the signals at time points (i) and (iii). These shifts were monitored at six odd-numbered overtones (n = 3, 5, 7, 9, 11, and 13) to assess adsorbed mass on the PEG layers. The adsorbed mass of the Fv-clasps was quantified using the Sauerbrey relation (Supporting Information S2). Following each measurement, the fluidic system was cleaned with 2% sodium dodecyl sulfate (SDS; Wako, Osaka, Japan), followed by rinsing with ultrapure water to ensure complete removal of residual proteins and surfactants. A separate series of QCM-D measurements were also performed to detect the real-time formation of the PEG SAMs onto the surface of the bare Au-coated quartz sensors. Solutions containing 1 mg/mL of m-PEG and HO-PEG in PBS were injected and equilibrated overnight to ensure the complete formation of the SAMs. Various parameters such as layer thickness, shear modulus and viscosity were calculated using QSense DFind software (v1.3.0) employing the Voigt viscoelastic model (Supporting Information S3). All other QCM-D analyses were processed using custom Python scripts (Python v3.10).

FTIR Measurements

FTIR spectra were collected using an FT/IR-6600 spectrometer (JASCO Inc., Tokyo, Japan) equipped with a diamond attenuated total reflectance (ATR) prism. Spectra were recorded over the wavenumber range of 4000−500 cm^{-1} with a resolution of 4 cm^{-1}. All measurements were performed at room temperature under a constant purge of dry nitrogen gas to minimize atmospheric interference. A background spectrum was first acquired using the clean ATR prism. Spectra were then obtained for the following samples: m-PEG and HO-PEG SAMs in both dry and hydrated states (in D_2O), to assess differences due to hydration. Additional measurements were taken for m-PEG and HO-PEG SAMs incubated with anti-PEG antibody Fv-clasps (M9 and M11) in the dry state to confirm successful binding. Following incubation, the substrates were rinsed thoroughly with PBS to remove unbound antibodies before analysis in the dry state. The spectra were normalized using the C−O−C band after ensuring identical incubation and washing conditions. For reference, dry-state spectra of PEG powder were also recorded. Three replicates were measured for each condition. The ATR prism was thoroughly cleaned with ethanol between measurements to prevent cross-contamination. All spectra were processed using custom Python scripts (Python v3.10).

RESULTS AND DISCUSSION

An overview of our integrated experimental strategy is presented in Figure 4, which frames the connection between single-molecule binding mechanics and interfacial or structural responses as revealed by ensemble techniques. We utilized SMFS as the primary approach to quantify PEG−antibody interactions at the single-molecule level, focusing on adhesion forces and rupture distances. Complementary ensemble measurements provided additional insights, with QCM-D probing the formation and hydration of PEG layers at interfaces and FTIR spectroscopy capturing conformational features of PEG and antibody binding.

Preliminary Ensemble Measurements

QCM-D measurements were conducted to quantify the binding interactions between anti-PEG antibody Fv-clasps and PEG SAMs with different terminal groups. The Fv-clasp is an engineered Fv fragment stabilized by a coiled-coil domain that promotes correct pairing of heavy and light chains, enabling immobilization at high density on substrate surfaces.[58] Specifically, Fv-clasps of naive (M9) and mutated (M11) antibody were introduced to gold sensors functionalized with PEG SAMs terminated with either hydroxy (HO-PEG) or methoxy (m-PEG) groups. Figure 5 presents representative real-time Δf profiles recorded during the injection of M9 and M11 onto the PEG-functionalized sensors.

The initial adsorption of the Fv-clasps onto the PEG-functionalized surfaces proceeded rapidly, with the majority of the frequency shift occurring within less than 5 min of Fv-clasp

https://doi.org/10.1021/acsabm.5c01967
ACS Appl. Bio Mater. 2026, 9, 1450−1462

injection. Notably, the magnitude of Δf observed for M11 was significantly greater than that of M9, irrespective of the PEG terminal group. These results reflect the enhanced affinity of the mutated M11 antibody toward PEG, as compared to the naïve M9 antibody.[38] To provide a quantitative comparison of the antibody−PEG binding, the bound mass of the Fv-clasps was calculated from Δf using the Sauerbrey equation. The resulting bound masses for each Fv-clasp−surface combination are summarized in Figure 6, which highlights the substantial

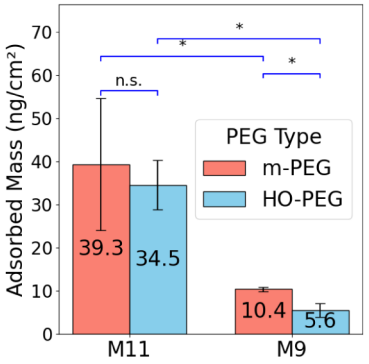

Figure 6. Adsorbed mass of Fv-clasp antibodies M11 and M9 on m-PEG and HO-PEG surfaces, calculated using the Sauerbrey equation at the seventh overtone. Error bars represent standard deviation (n = 3). Statistical significance: *p < 0.01; n.s. = not significant.

difference in binding between M11 and M9, as well as the influence of PEG terminal chemistry on antibody recognition. The amount of bound Fv-clasp was consistently greater for M11 than for M9 on both PEG surfaces, reflecting the typical difference in binding affinity between affinity-matured antibody and naïve one. M11 exhibited similar adsorption levels on m-PEG (39.3 ± 15.3 ng/cm^2) and HO-PEG (34.5 ± 5.7 ng/cm^2), consistent with previous reports indicating that M11 primarily recognizes the PEG backbone, rendering the terminal groups largely inconsequential to binding.[52] In contrast, M9 showed higher binding with m-PEG (10.4 ± 0.5 ng/cm^2), with significantly lower binding on HO-PEG (5.6 ± 1.6 ng/cm^2), which supports M9's preference to the terminal methoxy motif.[38,52]

To confirm that the Δf observed in QCM-D measurements arose from specific binding between the PEG molecules and the antibody Fv-clasps, we analyzed the PEG-functionalized substrates after Fv-clasp injection using FTIR spectroscopy. Figure 7 shows the normalized FTIR spectra of PEG SAMs injected with the two types of antibodies (m-PEG and HO-PEG with anti-PEG antibodies M11 and M9) in the dry state, recorded over the 1800−1000 cm^{-1} wavenumber region. The spectra display characteristic peaks at ∼1650 cm^{-1} and ∼1540 cm^{-1}, corresponding to the Amide I and Amide II vibrations, respectively, of the antibody Fv-clasps which confirm their successful binding to the PEG SAMs. In addition, M11 showed pronounced Amide I and Amide II peaks, further corroborating its reported higher binding affinity toward PEG compared to M9, which exhibited weaker and less distinct amide bands. These observations align well with previously reported ensemble measurements of anti-PEG antibodies interacting with PEG-functionalized surfaces, further supporting the distinct binding behaviors of naïve and affinity-matured constructs.

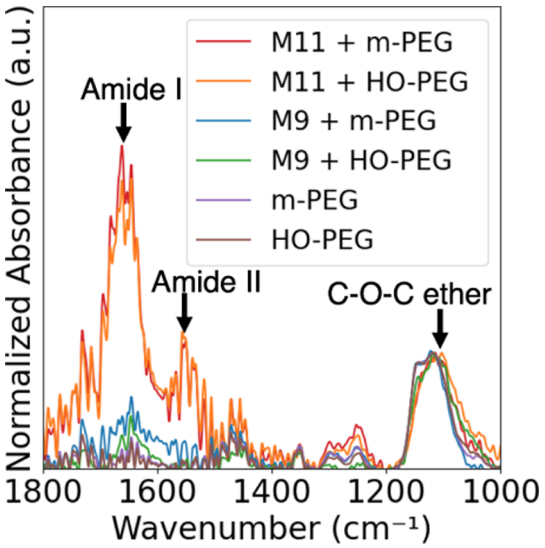

Figure 7. Normalized FTIR spectra of m-PEG and HO-PEG SAMs before and after incubation with anti-PEG antibody Fv-clasps (M9 and M11) in the dry state. Spectra highlight the emergence of protein-associated bands alongside the PEG backbone signature. Spectra of clean m-PEG and HO-PEG SAMs are included for comparison. All spectra were normalized using the C−O−C ether stretch peak (∼1095−1120 cm^{-1}) as a reference.

Single-Molecule Force Spectroscopy Experiments

To assess the molecular interactions between PEG and anti-PEG antibodies, we analyzed the distributions of adhesion forces obtained from AFM-SMFS, as shown in Figure 8. The results reveal clear differences in binding behavior based on both the antibody type and the PEG terminal group. Across both PEG types, the mutated antibody M11 consistently exhibited higher adhesion forces (28.12 pN against HO-PEG and 33.21 pN against m-PEG) compared to the naïve-type M9

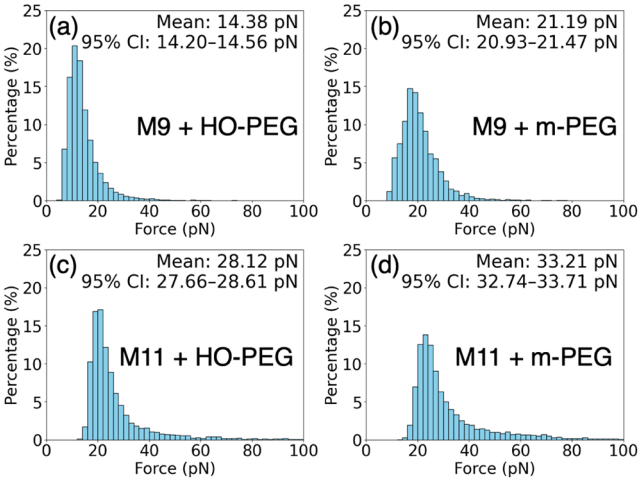

Figure 8. Histograms of adhesion force distributions for different antibody−PEG interactions. (a) M9 antibody interacting with HO-PEG, (b) M9 with m-PEG, (c) M11 with HO-PEG, and (d) M11 with m-PEG. Each histogram represents the distribution of unbinding forces collected from SMFS measurements. The mean adhesion forces were computed using bootstrapping due to non-normal distribution of the data. Variations in the force distributions reflect differences in binding strength and interaction profiles between antibody types and PEG terminal groups.

https://doi.org/10.1021/acsabm.5c01967
ACS Appl. Bio Mater. 2026, 9, 1450−1462

(14.38 pN against HO-PEG and 21.19 pN against m-PEG). These greater force values observed in our SMFS measurements suggest a stronger interaction between M11 and the PEG chains at the single-molecule level, reinforcing its reported superior recognition and affinity over M9.[38,62] M11, which was generated through the T-cell-dependent pathway, possesses higher binding affinity due to structural maturation in the complementarity-determining regions (CDRs).[63−65]

For both Fv-clasps, m-PEG yielded higher mean adhesion forces than HO-PEG. This trend was particularly pronounced for M9, which displayed significantly stronger binding to m-PEG suggesting that the methoxy terminus either promotes more frequent interactions or facilitates stronger binding events. This aligns with prior studies showing that M9 favors binding to m-PEG than HO-PEG.[52] Liu et al. reported from simulations that the PEG terminus interacts more frequently with certain hydrogen bond-forming residues in the M9 Fv-clasp.[38] They suggested that the hydrophobic methoxy group, rather than the hydroxy group, may better stabilize these contacts, thereby contributing to M9's preference for m-PEG over HO-PEG. Although our ensemble studies and other reports showed that M11 responds similarly to both m-PEG and HO-PEG, our SMFS results show a slight increase in adhesion force with m-PEG than HO-PEG (33.21 pN for m-PEG and 28.12 pN for HO-PEG). This discrepancy highlights the enhanced sensitivity of SMFS in detecting subtle differences in molecular binding strength that may be averaged out in bulk measurements.

Additionally, the observed differences in adhesion force may stem from how terminal chemistry influences PEG chain conformation. m-PEG chains, with more hydrophobic methoxy ends, are prone to loop formation in which the termini are partially buried, promoting tighter antibody engagement and higher rupture forces. In contrast, HO-PEG forms looser, more extended chains that remain more hydrated, leading to lower binding forces. This conformational effect is likely most pronounced for M9, which has lower intrinsic affinity and depends on PEG chain loops as the epitope. Further characterization of the m-PEG and HO-PEG molecules in the context of the differences in their hydrated structure is presented in detail later in this manuscript.

Next, we plotted the histograms for rupture distance distributions which offer insights into the spatial and mechanical aspects of antibody−PEG interactions at the single-molecule level, as shown in Figure 9. Notably, the rupture distance histograms exhibit a tail extending up to approximately 15 nm, which corresponds closely to the estimated fully extended contour length of a PEG2000 chain. Across all conditions, we observed that M11 (5.46 nm against HO-PEG and 5.19 nm against m-PEG) exhibited slightly shorter rupture distances than M9 (6.08 nm against HO-PEG and 5.42 nm against m-PEG). This suggests that M11 may form more compact and rigid binding complexes with PEG, resulting in earlier bond rupture under applied force. In contrast, M9 may permit greater extension prior to rupture, consistent with a more flexible interaction mechanism. In terms of terminal group effects, both Fv-clasps demonstrated slightly shorter rupture distances with m-PEG than with HO-PEG, albeit to varying extents. This trend may also be rationalized by the conformational behavior of the PEG termini. m-PEG's supposedly compact and collapsed structure may limit chain extension and facilitates tighter, more localized binding. When force is applied, these compact interactions

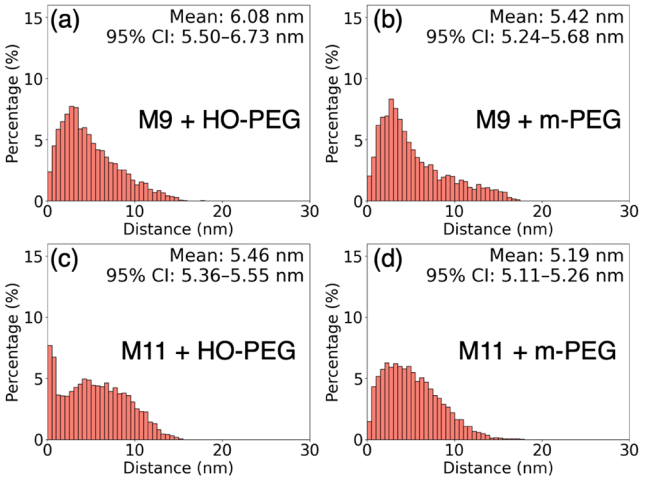

Figure 9. Histograms of rupture distance distributions for different antibody−PEG interactions. (a) M9 antibody with HO-PEG, (b) M9 with m-PEG, (c) M11 with HO-PEG, and (d) M11 with m-PEG. Rupture distances were extracted from AFM-based SMFS measurements and reflect the separation distance at which unbinding occurs. The mean rupture distances were computed using bootstrapping due to non-normal distribution of the data. Differences in rupture distances suggest variation in interaction geometry or flexibility between antibody types and PEG terminal groups.

rupture quickly, yielding shorter rupture distances. In contrast, HO-PEG's more extended and hydrated conformation may increase the effective chain length accessible for interaction. As a result, rupture events occur after more chain extension, leading to longer rupture distances.

To better resolve the molecular interaction profiles of PEG−antibody pairs, we analyzed two-dimensional kernel density estimation (2D-KDE) contour plots of adhesion force versus rupture distance, as shown in Figure 10. These plots reveal distinct interaction signatures for each pair, highlighting differences in binding strength and configurational dynamics. Among the M9 antibody interactions, M9 + HO-PEG exhibited a broadly distributed and the weakest binding profile. This broad, low-density region suggests flexible, low-affinity interactions characteristic of water-mediated binding with minimal spatial constraint. In contrast, M9 + m-PEG displayed a modest increase in both peak and mean adhesion forces, accompanied by an expanded hotspot area. These findings are consistent with the notion that the terminal methoxy group stabilizes interactions by reducing hydration competition, resulting in a moderately enhanced affinity while retaining a flexible interaction geometry.

For the mutated M11 antibody, both PEG types yielded significantly stronger adhesion signatures. M11 + HO-PEG exhibited a peak and mean forces, with a large hotspot area. These values indicate high-affinity interactions that may occur at different positions along the flexible PEG backbone. Notably, M11 + m-PEG produced the strongest interaction values. However, its hotspot area was the broadest among all conditions, suggesting that despite the increased strength and specificity toward the methoxy group, the binding landscape remains structurally heterogeneous.

Role of Antibody Structure in the PEG−Antibody Interaction

Our SMFS measurements revealed that antibody structure critically influences PEG binding. M11 exhibited consistently

https://doi.org/10.1021/acsabm.5c01967
ACS Appl. Bio Mater. 2026, 9, 1450−1462

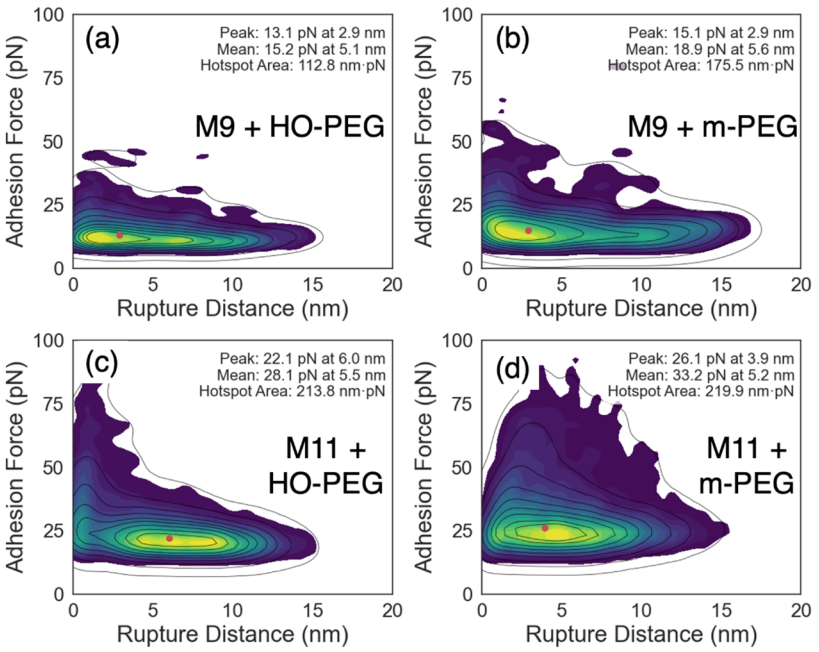

Figure 10. Kernel density estimation (KDE) contour maps of force−distance interactions between antibodies and PEGs. (a) M9 antibody interacting with HO-PEG, (b) M9 with m-PEG, (c) M11 with HO-PEG, and (d) M11 with m-PEG. Each contour map represents the density of unbinding events across rupture distance and force, as obtained from AFM-based SMFS. Denser regions (brighter contours) indicate frequent binding events, allowing comparison of interaction profiles between antibody types and PEG terminal groups.

higher adhesion forces and shorter rupture distances than M9, reflecting its affinity-matured, high-affinity interaction mode. KDE maps further supported this, showing concentrated high-force hotspots for M11−PEG interactions, while M9−PEG interactions displayed broader, lower-force distributions indicative of weaker and more flexible binding. Both antibodies favored m-PEG over HO-PEG, with M9 showing greater sensitivity to the terminal group. According to Liu et al., the crystal structure of M9-PEG complex shows PEG bound in a shallow pocket as a hairpin loop, with minimal hydrogen bonding, consistent with its lower affinity. In contrast, M11 binds PEG in a tunnel-like groove, stabilizing linear PEG chains through hydrophobic interactions.[38] The tunnel-like structure in M11 is formed by hydrophobic interactions between Tyr and Trp residues in CDR-H3 and CDR-H1, respectively. A Val−Ala insertion immediately upstream of the Tyr in CDR-H3 is the key mutation that induces this structural rearrangement. A similar tunnel structure was also observed in the crystal structure of another TD anti-PEG antibody clone.[33]

Moreover, molecular dynamics simulations revealed faster PEG sliding and shorter binding durations in M9, whereas M11 maintained prolonged binding with slower chain movement.[38] Notably, M9 interacted more frequently with the PEG terminal methoxy group through transient hydrogen bonds involving residues in the light chain CDRs, a feature largely absent in M11.[38] These molecular dynamics trends align with our SMFS results, supporting weaker binding for M9 and stronger binding for M11.

Role of PEG Hydrated Structure in the PEG−Antibody Interaction

From previous observations, the differences in adhesion force and rupture distance between PEG and anti-PEG antibodies (M9 and M11) were attributed to variations in the hydrated structures of m-PEG and HO-PEG molecules. Specifically, m-PEG is hypothesized to adopt a more collapsed or compact conformation, whereas HO-PEG is thought to form a more extended and hydrated structure. To support this hypothesis, FTIR measurements were conducted to probe differences in the hydrated states of m-PEG and HO-PEG SAMs. Figure 11a shows the normalized FTIR spectra of m-PEG and HO-PEG

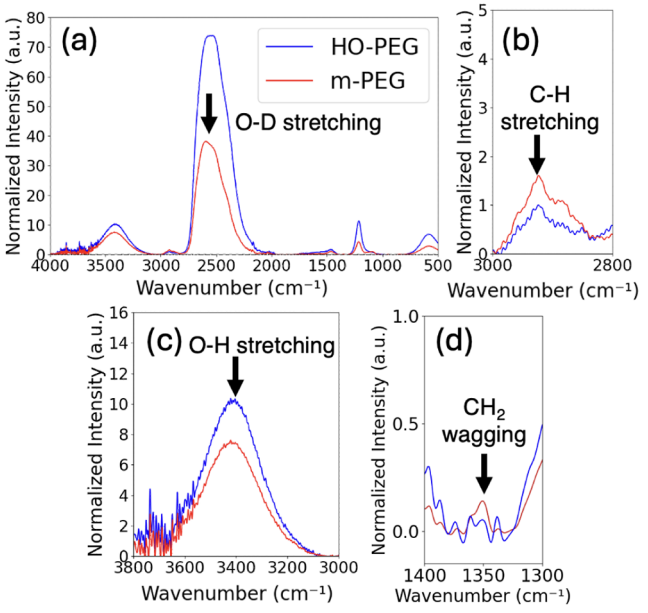

Figure 11. FTIR spectra of m-PEG and HO-PEG self-assembled monolayers (SAMs) in D_2O. (a) Full spectra over the wavenumber range of 4000−500 cm^{-1}. (b) Expanded view of the C−H stretching region (2950−2870 cm^{-1}), showing characteristic alkyl chain vibrations, (c) 3000−3800 cm^{-1} region, highlighting differences in the broadness and intensity of the O−H stretching band (3500−3200 cm^{-1}) and (d) CH_2 wagging/twisting vibrations (1340−1370 cm^{-1}), often associated with ordering of the PEG backbone.

https://doi.org/10.1021/acsabm.5c01967
ACS Appl. Bio Mater. 2026, 9, 1450−1462

SAMs in D_2O, with normalization performed using the C−O−C ether stretch peak (∼1095−1120 cm^{-1}) as an internal reference. The FTIR spectra of dry m-PEG and HO-PEG powders are also shown in the Supporting Information S4 for reference.

The OD stretching band at ∼2500 cm^{-1} was more intense for HO-PEG than for m-PEG, likely due to a greater exchange of the terminal −OH hydrogens with deuterium to form −OD in HO-PEG. In addition, only a subtle difference was observed in the C−H stretching region (2950−2870 cm^{-1}), as shown in Figure 11b, where m-PEG exhibited slightly stronger peak compared to HO-PEG, attributable to the minor contribution of the terminal methoxy ($-OCH_3$) group relative to the ∼45 ethylene glycol repeat units. Most notably, the O−H stretching band (3500−3200 cm^{-1}) for HO-PEG appeared significantly broader and more intense than that of m-PEG (Figure 11c). This broadening and increased intensity likely arise from ambient H_2O vapor partially re-exchanging deuterium back to hydrogen and may reflect the presence of a more extended hydration network around HO-PEG. Additional conformational information was obtained from the CH_2 wagging (∼1350 cm^{-1}) mode (Figure 11d). When normalized to the CH stretching band at ∼2950 cm^{-1}, this peak was more pronounced for HO-PEG compared to m-PEG, suggesting that HO-PEG chains adopt a more ordered helical backbone structure. Helical ordering is consistent with a more extended, hydrated chain conformation stabilized by hydrogen bonding with surrounding water molecules.[66,67] By contrast, the weaker intensity of these modes in m-PEG indicates a loss of helicity and greater conformational collapse, consistent with its compact, less hydrated layer, which may influence antibody binding.

To corroborate this interpretation, we next performed QCM-D measurements to directly probe the interfacial hydration and viscoelastic properties of the PEG SAMs. Specifically, QCM-D measurements were performed to monitor the real-time formation of PEG SAMs on gold-coated sensors. Representative real-time profiles of Δf vs time, ΔD vs time, and ΔD vs Δf are provided in the Supporting Information S5. The equilibrium Δf and ΔD values for m-PEG and HO-PEG SAMs across all overtones are summarized in Figure 12. Notably, the equilibrium Δf exhibited a substantial spread and a considerable ΔD values, indicative of the viscoelastic nature of the formed PEG layers.

To gain further insight into the physical and mechanical properties of the PEG layers, the QCM-D data were analyzed using a Voigt-based viscoelastic model. This modeling yielded estimates of the layer thickness, shear modulus, and viscosity, which are summarized in Table 2. The viscoelastic analysis showed that m-PEG SAMs formed relatively thinner layers with higher shear modulus and viscosity, whereas HO-PEG SAMs formed thicker and softer layers. These differences in thickness and mechanical properties are probably due to the conformational changes of PEG molecules during the SAM formation, associated with the release of internal water from within the molecular structure as indicated by the positive Δf. HO-PEG exhibited a more substantial positive shift in Δf immediately after the injection of PEG solutions as compared to m-PEG (Supporting Information S6), consistent with its higher hydrophilicity due to the hydroxy terminal group. This enhanced water affinity accounts for the formation of a more extended and hydrated HO-PEG layer compared to the more compact m-PEG layer. The calculated thickness, shear modulus, and viscosity consistently support the hypothesis regarding the differences in the hydrated structures of m-PEG and HO-PEG molecules which highly impacted how anti-PEG antibodies bind to PEG molecule with different terminal motifs. However, we caution that the absolute values derived from Voigt modeling depend on simplifying assumptions regarding homogeneity, layer uniformity, and bulk-like viscoelastic response. Differences in surface coverage or adsorption kinetics may also contribute to the observed trends and cannot be fully decoupled from hydration effects.

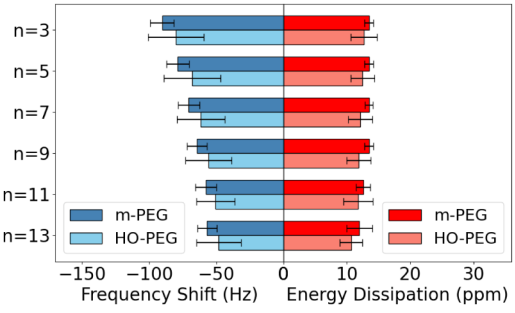

Figure 12. Equilibrium Δf (left) and ΔD (right) from the formation of m-PEG and HO-PEG SAMs, measured at overtones 3, 5, 7, 9, 11, and 13. Error bars denote standard deviation (n = 6).

Table 2. Parameters Obtained from the QCM-D Data Using the Viscoelastic (Voigt Fitting) Model

Type of PEG SAMs	Layer thickness (nm)[a]	Shear modulus (kPa)[b]	Viscosity (μPa s)[c]
m-PEG SAM	4.5 (0.1)	19.6 (2.6)	1635 (25)
HO-PEG SAM	4.7 (0.2)	10.4 (4.7)	1499 (91)

[a]Numbers in parentheses denote standard deviation (n = 6). Statistical significance. [b]$p < 0.1$. [c]$p < 0.01$.

Collectively, our findings support the conclusion that m-PEG adopts a more compact and less hydrated configuration than HO-PEG. Previous studies have reported that m-PEG exhibits a higher probability of chain backfolding or loop-like conformations compared with hydroxy-terminated PEG.[68−70] Consistent with these reports, our QCM-D and FTIR measurements show that m-PEG forms a thinner, less hydrated, and more viscoelastic layer than HO-PEG. The shorter rupture distances observed in SMFS further support that a subset of m-PEG chains adopt less extended conformations under our experimental conditions. Although AFM-SMFS does not directly visualize loop geometries, the combination of theoretical expectations, literature reports, and our multimodal measurements indicates that loop-like behavior is plausible under the conditions of this study.

Proposed Model of PEG−Antibody Interactions

In AFM-SMFS, the Fv-clasp antibodies were covalently coupled to COOH-terminated alkanethiol SAMs via EDC/NHS chemistry. This conjugation strategy is widely used for immobilizing proteins on gold surfaces and preserves their structural integrity and biological activity, while generating an orientationally heterogeneous ensemble that avoids artificial geometric constraints.[60,71] PEG chains on the AFM tip were attached through thiol−gold chemistry, a well-established approach known to maintain native PEG chain flexibility, dynamics, and hydration and experimentally validated on

https://doi.org/10.1021/acsabm.5c01967
ACS Appl. Bio Mater. 2026, 9, 1450−1462

SAM-modified gold.[72,73] Consistent with these expectations, our QCM-D viscoelastic modeling and FTIR analysis confirmed that m-PEG and HO-PEG layers exhibit their anticipated differences in thickness, hydration state, and configuration, indicating that immobilization does not impose abnormal conformational distortion. Despite differing immobilization geometries across AFM-SMFS, QCM-D, and FTIR, all three modalities consistently show enhanced binding to less hydrated m-PEG and suppressed recognition of highly hydrated HO-PEG. These results are also in agreement with previous SPR and ELISA measurements in solution,[74,75] suggesting that the single-molecule behavior observed here reflects intrinsic PEG−antibody recognition rather than an artifact of surface attachment.

We converge our combined findings from AFM-SMFS, FTIR spectroscopy, and QCM-D measurements into a mechanistic model describing how antibody structure and PEG terminal chemistry govern PEG−antibody interactions, as illustrated in Figure 13. In this model, m-PEG adopts a compact, collapsed conformation with reduced hydration, while HO-PEG forms an extended and hydrated layer at the interface. These conformational differences modulate the accessibility of PEG chains to antibodies.

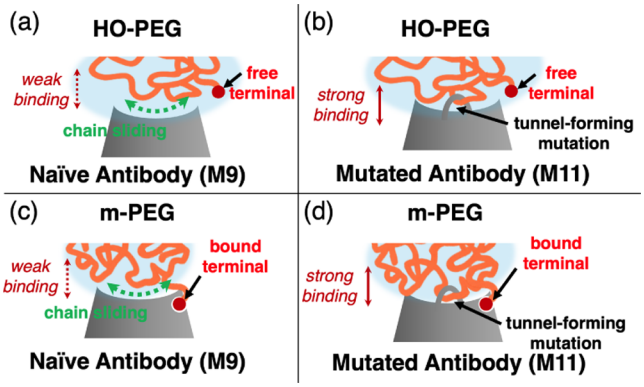

Figure 13. Proposed mechanistic model of PEG−antibody interactions derived from AFM-SMFS, FTIR, and QCM-D. (a) M9 (naïve) engages PEG through a shallow binding pocket, resulting in weak interactions dominated by chain sliding. (b) M11 (mutated) contains tunnel-forming mutations that stabilize linear PEG chains and produce consistently stronger binding. Both antibodies interact with the methoxy terminus; however, while ensemble measurements indicated terminal sensitivity primarily for M9, the higher resolution of SMFS revealed terminal interactions for both M9 (c) and M11 (d).

For M9, which binds PEG through a shallow binding pocket, interactions are relatively weak and often comprised by chain sliding. Consequently, its binding is highly sensitive to PEG terminal chemistry and conformation, i.e., compact m-PEG provides more favorable termini for interaction, while the extended hydration network of HO-PEG reduces accessibility and weakens binding. In contrast, M11 contains tunnel-forming mutations that stabilize linear PEG chains within a groove, producing consistently stronger and more localized interactions across terminal chemistries. Ensemble measurements emphasized the methoxy terminal group dependence primarily for M9, but the higher sensitivity of SMFS revealed that methoxy interactions also contribute to M11 binding.

We provide a unified mechanistic framework in which PEG hydration state and antibody structural features jointly determine binding strength, specificity, and molecular dynamics. This integrated model highlights how hydration-mediated polymer conformations and antibody structural maturation intersect to define PEG recognition. These single-molecule insights have direct implications for PEGylated nanomedicines, where balancing long-circulating "stealth" behavior with efficient targeting remains a central design challenge.[76] Recent work has emphasized that the clinical performance of PEGylated nanoparticles is strongly influenced by how their surface chemistry modulates interactions with antibodies and serum proteins. Our results suggest that densely PEGylated nanocarriers bearing methoxy-terminated PEG may present localized "hot spots" for anti-PEG recognition in patients with preexisting antibodies, potentially accelerating clearance, whereas more hydrated terminal groups or mixed/hybrid stealth coatings could reduce immunogenic recognition. In a broader context, the hydration-dependent accessibility of PEG observed here may serve as a design principle not only for optimizing PEG architectures, but also for engineering alternative stealth polymers (e.g., zwitterionic or PEG-alternative hydrophilic chains) that better evade antibody binding while maintaining favorable pharmacokinetics.

SUMMARY AND CONCLUSION

In this study, we investigated the interaction mechanisms between anti-PEG antibody Fv-clasps and PEG molecules terminated with hydroxy or methoxy groups, using AFM-SMFS, QCM-D, and FTIR spectroscopy measurements. This multiscale approach allowed us to correlate the molecular binding behavior of anti-PEG antibodies with the structural and mechanical properties of the underlying PEG molecules.

QCM-D ensemble measurements confirmed that the mutated antibody M11 consistently exhibited higher binding to PEG SAMs than the naïve-type M9, reflecting the role of affinity maturation in enhancing molecular recognition. M11 binding was largely independent of terminal chemistry, showing similar binding to m-PEG and HO-PEG, consistent with its reported backbone recognition. In contrast, M9 displayed a clear preference for m-PEG than HO-PEG, indicative of its sensitivity to terminal group chemistry. FTIR analysis of PEG−Fv-clasp complexes supported these findings by revealing more pronounced Amide I and Amide II signals for M11 compared to M9. AFM-SMFS further demonstrated that M11 bound more strongly to PEG than M9, consistent with its reported higher affinity as an affinity-matured antibody. Both antibodies exhibited stronger adhesion to m-PEG than HO-PEG, with M9 showing a more pronounced terminal preference. Rupture distance analysis distinguished their binding mechanics, wherein M9 showed longer rupture distances, characteristic of flexible, low-affinity interactions, while M11 exhibited shorter rupture distances indicative of strong, localized binding. 2D-KDE plots of force versus distance revealed broad, low-force distributions for M9−HO-PEG interactions, consistent with weak, water-mediated binding. M11−PEG interactions displayed high-affinity binding with broad hotspot areas, suggesting the presence of multiple binding modes involving both terminal and backbone engagement. To understand how the structural and hydration properties of PEG molecules influence these interactions, we characterized the hydrated states of m-PEG and HO-PEG using FTIR and QCM-D. FTIR spectra in D_2O revealed that HO-PEG exhibited broader and more intense O−H stretching bands and more prominent O−D bands, indicating a more extended hydration network compared to m-PEG. QCM-D

https://doi.org/10.1021/acsabm.5c01967
ACS Appl. Bio Mater. 2026, 9, 1450−1462

measurements of PEG SAM formation, analyzed via viscoelastic modeling, showed that m-PEG formed thinner, stiffer, and more viscous layers, consistent with a compact, collapsed conformation whereas HO-PEG formed thicker, softer, and more dynamic layers, indicative of an extended and hydrated structure. The compact and less hydrated structure of m-PEG favors localized, high-affinity binding while the extended, hydrated HO-PEG layer reduces binding, especially for the naïve M9 antibody.

These findings highlight how both antibody maturation and PEG terminal chemistry influence the strength, spatial characteristics, and modes of PEG−antibody interactions. Although methoxy terminals are commonly favored in PEGylated drugs for their chemical stability, our results show that they may increase recognition by anti-PEG antibodies. In contrast, hydroxy terminals, though more chemically reactive, appear less immunogenic in SMFS measurements. These insights deepen our understanding of the molecular determinants of anti-PEG recognition and have important implications for the rational design of PEGylated therapeutics with reduced immunogenicity and improved biocompatibility. To achieve both chemical stability and immune invisibility, future stealth polymers may need to decouple these properties through more refined molecular designs.

■ ASSOCIATED CONTENT

Supporting Information

The Supporting Information is available free of charge at https://pubs.acs.org/doi/10.1021/acsabm.5c01967.

Preliminary determination of the optimal antibody concentration; conventional mass loading by Sauerbrey relation; viscoelastic modeling of QCM-D data; FTIR spectra of dry m-PEG and HO-PEG powders; representative real-time profiles of Δf vs time, ΔD vs time, and ΔD vs Δf; estimation of released water by PEG molecules in SAM formation from changes in Δf (PDF)

■ AUTHOR INFORMATION

Corresponding Authors

Takeshi Mori − *Department of Applied Chemistry, Faculty of Engineering, Kyushu University, Fukuoka 819-0395, Japan;* orcid.org/0000-0002-1821-5427; Email: mori.takeshi.880@m.kyushu-u.ac.jp

Tomohiro Hayashi − *Department of Materials Science and Engineering, School of Materials and Chemical Technology, Institute of Science Tokyo, Yokohama, Kanagawa 226-8502, Japan;* orcid.org/0000-0002-4065-1807; Email: th@mct.isct.ac.jp

Authors

Glenn Villena Latag − *Department of Materials Science and Engineering, School of Materials and Chemical Technology, Institute of Science Tokyo, Yokohama, Kanagawa 226-8502, Japan;* orcid.org/0009-0009-3839-546X

Hiroyuki Tahara − *Department of Materials Science and Engineering, School of Materials and Chemical Technology, Institute of Science Tokyo, Yokohama, Kanagawa 226-8502, Japan*

Airi Katase − *Department of Materials Science and Engineering, School of Materials and Chemical Technology, Institute of Science Tokyo, Yokohama, Kanagawa 226-8502, Japan*

Shoichi Maeda − *Department of Materials Science and Engineering, School of Materials and Chemical Technology, Institute of Science Tokyo, Yokohama, Kanagawa 226-8502, Japan*

Yiwei Liu − *Department of Applied Chemistry, Faculty of Engineering, Kyushu University, Fukuoka 819-0395, Japan;* orcid.org/0000-0002-8072-0715

Yoshimitsu Kakuta − *Department of Bioscience and Biotechnology, Faculty of Agriculture, Kyushu University, Fukuoka 819-0395, Japan*

Takamasa Teramoto − *Department of Bioscience and Biotechnology, Faculty of Agriculture, Kyushu University, Fukuoka 819-0395, Japan*

Complete contact information is available at: https://pubs.acs.org/10.1021/acsabm.5c01967

Author Contributions

The manuscript was written through the contributions of all authors. All authors have approved the final version of the manuscript.

Funding

This work was supported by MEXT/JSPS KAKENHI Grant Numbers (JP23H04059, JP22H04530, JP20H05876, and JP24K21337). This work was performed under the Research Program for CORE lab of "Five-star Alliance" in "NJRC Mater. & Dev.". This work was also supported by the Japan−Taiwan Exchange Association (International Collaboration Program). This work was supported by the Innovative Science and Technology Initiative for Security (ISTIS), Acquisition, Technology & Logistics Agency (ATLA), Japan (Grant Number JPJ013268).

Notes

The authors declare no competing financial interest.

■ ACKNOWLEDGMENTS

We thank Ms. Kazue Taki for the administration of this project.

■ REFERENCES

(1) Mitchell, M. J.; et al. Engineering precision nanoparticles for drug delivery. *Nat. Rev. Drug Discovery* **2021**, *20*, 101−124.

(2) Wu, D.; Chen, Q.; Chen, X.; Han, F.; Chen, Z.; Wang, Y. The blood-brain barrier: structure, regulation, and drug delivery. *Signal Transduct. Target. Ther.* **2023**, *8*, 217.

(3) Ezike, T. C.; et al. Advances in drug delivery systems, challenges and future directions. *Heliyon* **2023**, *9*, No. e17488.

(4) Rahban, M.; et al. Stabilization challenges and aggregation in protein-based therapeutics in the pharmaceutical industry. *RSC Adv.* **2023**, *13*, 35947−35963.

(5) Lee, Y.; Jeong, M.; Park, J.; Jung, H.; Lee, H. Immunogenicity of lipid nanoparticles and its impact on the efficacy of mRNA vaccines and therapeutics. *Exp. Mol. Med.* **2023**, *55*, 2085−2096.

(6) Grabbe, S.; Landfester, K.; Schuppan, D.; Barz, M.; Zentel, R. Nanoparticles and the immune system: challenges and opportunities. *Nanomedicine* **2016**, *11*, 2621−2624.

(7) Fam, S. Y.; et al. Stealth coating of nanoparticles in drug-delivery systems. *Nanomaterials* **2020**, *10*, 787.

(8) Ly, P. D.; Ly, K. N.; Phan, H. L.; Nguyen, H. H.; Duong, V. A.; Nguyen, H. V. Recent advances in surface decoration of nanoparticles in drug delivery. *Front. Nanotechnol.* **2024**, *6*, 1456939.

(9) Graván, P.; et al. Exploring the impact of nanoparticle stealth coatings in cancer models: From PEGylation to cell membrane-coating nanotechnology. *ACS Appl. Mater. Interfaces* **2024**, *16*, 2058−2074.
(10) Schneck, E.; Berts, I.; Halperin, A.; Daillant, J.; Fragneto, G. Neutron reflectometry from poly (ethylene-glycol) brushes binding anti-PEG antibodies: evidence of ternary adsorption. *Biomaterials* **2015**, *46*, 95−104.
(11) Jahani, A.; Nassira, H. Polyethylene glycol-based materials: Transformative applications in biomedicine and the food industry. *Mater. Chem. Horiz.* **2024**, *3*, 1−25.
(12) Truong, V.; Blakey, I.; Whittaker, A. K. Hydrophilic and amphiphilic polyethylene glycol-based hydrogels with tunable degradability prepared by "click" chemistry. *Biomacromolecules* **2012**, *13*, 4012−4021.
(13) Zhao, X.; et al. Application of star poly(ethylene glycol) derivatives in drug delivery and controlled release. *J. Controlled Release* **2020**, *323*, 565−577.
(14) Milla, P.; Dosio, F.; Cattel, L. PEGylation of proteins and liposomes: a powerful and flexible strategy to improve the drug delivery. *Curr. Drug Metab.* **2012**, *13*, 105−119.
(15) Knop, K.; Hoogenboom, R.; Fischer, D.; Schubert, U. S. Poly(ethylene glycol) in drug delivery: pros and cons as well as potential alternatives. *Angew. Chem., Int. Ed.* **2010**, *49*, 6288−6308.
(16) Yang, Q.; et al. Evading immune cell uptake and clearance requires PEG grafting at densities substantially exceeding the minimum for brush conformation. *Mol. Pharmaceutics* **2014**, *11*, 1250−1258.
(17) Li, M.; et al. Brush conformation of polyethylene glycol determines the stealth effect of nanocarriers in the low protein adsorption regime. *Nano Lett.* **2021**, *21*, 1591−1598.
(18) Du, H.; Chandaroy, P.; Hui, S. W. Grafted poly-(ethylene glycol) on lipid surfaces inhibits protein adsorption and cell adhesion. *Biochim. Biophys. Acta* **1997**, *1326*, 236−248.
(19) Mehta, P.; Shende, P. Evasion of opsonization of macromolecules using novel surface-modification and biological-camouflage-mediated techniques for next-generation drug delivery. *Cell Biochem. Funct.* **2023**, *41*, 1031−1043.
(20) Sroda, K.; Rydlewski, J.; Langner, M.; Kozubek, A.; Grzybek, M. Repeated injections of PEG-PE liposomes generate anti-PEG antibodies. *Cell. Mol. Biol. Lett.* **2005**, *10*, 37−47.
(21) Chen, B.-M.; Cheng, T.-L.; Roffler, S. R. Polyethylene Glycol Immunogenicity: Theoretical, Clinical, and Practical Aspects of Anti-Polyethylene Glycol Antibodies. *ACS Nano* **2021**, *15*, 14022−14048.
(22) Kozma, G. T.; Shimizu, T.; Ishida, T.; Szebeni, J. Anti-PEG antibodies: Properties, formation, testing and role in adverse immune reactions to PEGylated nano-biopharmaceuticals. *Adv. Drug Delivery Rev.* **2020**, *154*−*155*, 163−175.
(23) Yang, Q.; Lai, S. K. Anti-PEG immunity: emergence, characteristics, and unaddressed questions. *Wiley Interdiscip. Rev. Nanomed. Nanobiotechnol.* **2015**, *7*, 655−677.
(24) Ju, Y.; et al. Impact of anti-PEG antibodies induced by SARS-CoV-2 mRNA vaccines. *Nat. Rev. Immunol.* **2023**, *23*, 135−136.
(25) Verhoef, J. J. F.; Carpenter, J. F.; Anchordoquy, T. J.; Schellekens, H. Potential induction of anti-PEG antibodies and complement activation toward PEGylated therapeutics. *Drug Discovery Today* **2014**, *19*, 1945−1952.
(26) Chang, T.-C.; Chen, B.-M.; Wu, J.-Y.; Cheng, T.-L.; Roffler, S. Impact of anti-PEG antibody affinity on accelerated blood clearance of pegylated epoetin beta in mice. *Biomed. Pharmacother.* **2022**, *146*, 112502.
(27) Moreno, A.; Pitoc, G. A.; Ganson, N. J.; Layzer, J. M.; Hershfield, M. S.; Tarantal, A. F.; Sullenger, B. A. Anti-PEG antibodies inhibit the anticoagulant activity of PEGylated aptamers. *Cell Chem. Biol.* **2019**, *26*, 634−644.e3.
(28) Siebel, C.; et al. Impact of antibodies against polyethylene glycol on the pharmacokinetics of PEGylated asparaginase in children with acute lymphoblastic leukaemia: A population pharmacokinetic approach. *Eur. J. Drug Metab. Pharmacokinet.* **2022**, *47*, 187−198.
(29) Khalil, A.; et al. Pre-existing antibodies against polyethylene glycol reduce asparaginase activities on first administration of pegylated *E. coli* asparaginase in children with acute lymphocytic leukemia. *Haematologica* **2022**, *107*, 49−57.
(30) Zhang, P.; et al. Sensitive and quantitative detection of anti-poly(ethylene glycol) (PEG) antibodies by methoxy-PEG-coated surface plasmon resonance sensors. *Anal. Chem.* **2017**, *89*, 8217−8222.
(31) Ju, Y.; et al. Anti-PEG Antibodies Boosted in Humans by SARS-CoV-2 Lipid Nanoparticle mRNA Vaccine. *ACS Nano* **2022**, *16*, 11769−11780.
(32) Mostafa, M.; et al. Using Bio-Layer Interferometry to Evaluate Anti-PEG Antibody-Mediated Complement Activation. *Biol. Pharm. Bull.* **2022**, *45*, 129−135.
(33) Huckaby, J. T.; Jacobs, T. M.; Li, Z.; Perna, R. J.; Wang, A.; Nicely, N. I.; Lai, S. K. Structure of an anti-PEG antibody reveals an open ring that captures highly flexible PEG polymers. *Commun. Chem.* **2020**, *3*, 124.
(34) Lee, C. C.; Su, Y. C.; Ko, T. P.; Lin, L. L.; Yang, C. Y.; Chang, S. S. C.; Roffler, S. R.; Wang, A. H. J. Structural basis of polyethylene glycol recognition by antibody. *J. Biomed. Sci.* **2020**, *27*, 12.
(35) Suzuki, T.; et al. PEG shedding-rate-dependent blood clearance of PEGylated lipid nanoparticles in mice: Faster PEG shedding attenuates anti-PEG IgM production. *Int. J. Pharm.* **2020**, *588*, 119792.
(36) Chen, E.; et al. Premature Drug Release from Polyethylene Glycol (PEG)-Coated Liposomal Doxorubicin via Formation of the Membrane Attack Complex. *ACS Nano* **2020**, *14*, 7808−7822.
(37) Ishida, T.; Wang, X.; Shimizu, T.; Nawata, K.; Kiwada, H. PEGylated liposomes elicit an anti-PEG IgM response in a T cell-independent manner. *J. Controlled Release* **2007**, *122*, 349−355.
(38) Liu, Y.; et al. The strategy used by naïve anti-PEG antibodies to capture flexible and featureless PEG chains. *J. Controlled Release* **2025**, *380*, 396−403.
(39) Takata, H.; et al. Anti-PEG IgM production induced by PEGylated liposomes as a function of administration route. *J. Controlled Release* **2023**, *360*, 285−292.
(40) Ichihara, M.; et al. Anti-PEG IgM response against PEGylated liposomes in mice and rats. *Pharmaceutics* **2011**, *3*, 1−11.
(41) Shiraishi, K.; Yokoyama, M. Antigenicity extension: A novel concept explained by the immunogenicity of PEG. *ACS Bio Med. Chem. Au* **2025**, *5*, 42.
(42) Chen, W.-A.; et al. Antibodies against poly(ethylene glycol) activate innate immune cells and induce hypersensitivity reactions to PEGylated nanomedicines. *ACS Nano* **2023**, *17*, 5757−5772.
(43) Vasquez, P. A.; et al. The power of weak, transient interactions across biology: A paradigm of emergent behavior. *Phys. D* **2023**, *454*, 133866.
(44) Mondarte, E. A. Q.; et al. Lab on a tip: Atomic force microscopy as a versatile analytical tool for nano-bioscience. *Sens. Mater.* **2021**, *33*, 223.
(45) Maekawa, T.; et al. Visualization of molecular binding sites at the nanoscale in the lift-up mode by amplitude-modulation atomic force microscopy. *Nanoscale* **2021**, *13*, 4213−4220.
(46) Tahara, H.; Nyu, T.; Mondarte, E. A.; Maekawa, T.; Hayashi, T. Application of fuzzy logic algorithm to single-molecule force spectroscopy of the streptavidin-biotin system. *Adv. Mater. Phy. Chem.* **2018**, *8*, 217−226.
(47) Arai, Y.; Okabe, K.-I.; Sekiguchi, H.; Hayashi, T.; Hara, M. Nanoscale chemical composition analysis using peptides targeting inorganic materials. *Langmuir* **2011**, *27*, 2478−2483.
(48) Idiris, A.; et al. Force Measurement for Antigen−Antibody Interaction by Atomic Force Microscopy Using a Photograft-Polymer Spacer. *Biomacromolecules* **2005**, *6*, 2776−2784.
(49) Li, M.; Dang, D.; Liu, L.; Xi, N.; Wang, Y. Imaging and Force Recognition of Single Molecular Behaviors Using Atomic Force Microscopy. *Sensors* **2017**, *17*, 200.

https://doi.org/10.1021/acsabm.5c01967
ACS Appl. Bio Mater. 2026, 9, 1450−1462

(50) Takechi-Haraya, Y.; Usui, A.; Izutsu, K.-I.; Abe, Y. Atomic Force Microscopic Imaging of mRNA-lipid Nanoparticles in Aqueous Medium. *J. Pharm. Sci.* **2023**, *112*, 648.
(51) Viljoen, A.; Mathelié-Guinlet, M.; Ray, A.; Strohmeyer, N.; Oh, Y. J.; Hinterdorfer, P.; Müller, D. J.; Alsteens, D.; Dufrêne, Y. F. Force spectroscopy of single cells using atomic force microscopy. *Nat. Rev. Methods Primers* **2021**, *1*, 63.
(52) Hashimoto, Y.; et al. Generation, characterization and in vivo biological activity of two distinct monoclonal anti-PEG IgMs. *Toxicol. Appl. Pharmacol.* **2014**, *277*, 30−38.
(53) Sherman, M. R.; Williams, L. D.; Sobczyk, M. A.; Michaels, S. J.; Saifer, M. G. P. Role of the methoxy group in immune responses to mPEG-protein conjugates. *Bioconjugate Chem.* **2012**, *23*, 485−499.
(54) Kim, H.; Hoshi, M.; Iijima, M.; Kuroda, S.; Nakamura, C. Development of a universal method for the measurement of binding affinities of antibody drugs towards a living cell based on AFM force spectroscopy. *Anal. Methods* **2020**, *12*, 2922−2927.
(55) Qin, J.; et al. Imaging and quantifying analysis the binding behavior of PD-L1 at molecular resolution by atomic force microscopy. *Anal. Chim. Acta* **2022**, *1191*, 339281.
(56) Hayashi, T.; Latag, G. V. Self-assembled monolayers as platforms for nanobiotechnology and biointerface research: Fabrication, analysis, mechanisms, and design. *ACS Appl. Nano Mater.* **2025**, *8*, 8570.
(57) Hayashi, T.; Tanaka, Y.; Koide, Y.; Tanaka, M.; Hara, M. Mechanism underlying bioinertness of self-assembled monolayers of oligo(ethyleneglycol)-terminated alkanethiols on gold: protein adsorption, platelet adhesion, and surface forces. *Phys. Chem. Chem. Phys.* **2012**, *14*, 10196−10206.
(58) Arimori, T.; Kitago, Y.; Umitsu, M.; Fujii, Y.; Asaki, R.; Tamura-Kawakami, K.; Takagi, J. Fv-clasp: An Artificially Designed Small Antibody Fragment with Improved Production Compatibility, Stability, and Crystallizability. *Structure* **2017**, *25*, 1611−1622.e4.
(59) Butt, H.-J.; Cappella, B.; Kappl, M. Force measurements with the atomic force microscope: Technique, interpretation and applications. *Surf. Sci. Rep.* **2005**, *59*, 1−152.
(60) Becke, T. D.; Ness, S.; Sudhop, S.; Gaub, H. E.; Hilleringmann, M.; Schilling, A. F.; Clausen-Schaumann, H. Covalent Immobilization of Proteins for the Single Molecule Force Spectroscopy. *J. Vis. Exp.* **2018**, 58167.
(61) Latag, G. V.; Nakamura, T.; Palai, D.; Mondarte, E. A. Q.; Hayashi, T. Investigation of Three-Dimensional Bacterial Adhesion Manner on Model Organic Surfaces Using Quartz Crystal Microbalance with Energy Dissipation Monitoring. *ACS Appl. Bio Mater.* **2023**, *6*, 1185−1194.
(62) Hori, T.; Shimizu, T.; Ando, H.; Okada, N.; Yamagami, H.; Yasui, S.; Hosoki, M.; Tojima, A.; Otoda, T.; Yuasa, T.; et al. Humoral Immune Response Against SARS-CoV-2 and Polyethylene Glycol Elicited by Anti-SARS-CoV-2 mRNA Vaccine in Patients with Hematological and Autoimmune Disease. *Heliyon* **2024**, *10*, No. e31489.
(63) Jeliazkov, J. R.; Sljoka; Kuroda, A.; Tsuchimura, D.; Katoh, N.; Tsumoto, N.; Gray, K. Repertoire analysis of antibody CDR-H3 loops suggests affinity maturation does not typically result in rigidification. *Front. Immunol.* **2018**, *9*, 413.
(64) Sheng, Z.; Bimela, J. S.; Katsamba, P. S.; Patel, S. D.; Guo, Y.; Zhao, H.; Guo, Y.; Kwong, P. D.; Shapiro, L. Structural basis of antibody conformation and stability modulation by framework somatic hypermutation. *Front. Immunol.* **2021**, *12*, 811632.
(65) Tiller, K. E.; et al. Arginine mutations in antibody complementarity-determining regions display context-dependent affinity/specificity trade-offs. *J. Biol. Chem.* **2017**, *292*, 16638−16652.
(66) Alessi, M. L.; Norman, A. I.; Knowlton, S. E.; Ho, D. L.; Greer, S. C. Helical and coil conformations of poly(ethylene glycol) in isobutyric acid and water. *Macromolecules* **2005**, *38*, 9333−9340.
(67) Rubinson, K. A.; Meuse, C. W. Deep hydration: Poly(ethylene glycol) Mw 2000−8000 Da probed by vibrational spectrometry and small-angle neutron scattering and assignment of ΔG° to individual water layers. *Polymer* **2013**, *54*, 709−723.
(68) Fuchs, P. F. J.; Hansen, H. S.; Hünenberger, P. H.; Horta, B. A. C. A GROMOS Parameter Set for Vicinal Diether Functions: Properties of Polyethyleneoxide and Polyethyleneglycol. *J. Chem. Theory Comput.* **2012**, *8*, 3943−3963.
(69) Currie, E. P. K.; Norde, W.; Cohen Stuart, M. A. Tethered polymer chains: surface chemistry and their impact on colloidal and surface properties. *Adv. Colloid Interface Sci.* **2003**, *100−102*, 205−265.
(70) Jeon, S. I.; Lee, J. H.; Andrade, J. D.; De Gennes, P. G. Protein—surface interactions in the presence of polyethylene oxide. *J. Colloid Interface Sci.* **1991**, *142*, 149−158.
(71) Stillger, L.; Müller, D. Peptide-coating combating antimicrobial contaminations: a review of covalent immobilization strategies for industrial applications. *J. Mater. Sci.* **2022**, *57*, 10863−10885.
(72) Morfill, J.; et al. Affinity-matured recombinant antibody fragments analyzed by single-molecule force spectroscopy. *Biophys. J.* **2007**, *93*, 3583−3590.
(73) Ros, R.; et al. Antigen binding forces of individually addressed single-chain Fv antibody molecules. *Proc. Natl. Acad. Sci. U. S. A.* **1998**, *95*, 7402−7405.
(74) Nguyen, M. -T. T.; Shih, Y. -C.; Lin, M. -H.; Roffler, S. -R.; Hsiao, C. -Y.; Cheng, T. -L.; Lin, W. -W.; Lin; Jong, E. -C.; Chang, Y. -J.; et al. Structural determination of an antibody that specifically recognizes polyethylene glycol with a terminal methoxy group. *Commun. Chem.* **2022**, *5*, 88.
(75) Shimizu, T.; Lila, A. S. A.; Awata, M.; Kubo, Y.; Yu, M.; Hashimoto, Y.; Ando, H.; Okuhira, K.; Ishima, Y.; Ishida, T. A cell assay for detecting anti-PEG immune response against PEG-modified therapeutics. *Pharm. Res.* **2018**, *35*, 223.
(76) Ju, Y.; Kent, S. J. Balancing stealth and targeting to improve nanomedicine efficacy. *Nat. Nanotechnol.* **2025**, *20*, 576−579.

https://doi.org/10.1021/acsabm.5c01967
ACS Appl. Bio Mater. 2026, 9, 1450−1462